Supplemental Material

Hydrogen network modes in liquid water

David P. Shelton

1. Temperature at the laser beam focus.

2. Polarization analysis with large collection aperture.

3. HRS spectra and fit functions.

References

[1] S. Kedenburg, M. Vieweg, T. Gissibl, and H. Giessen, Linear refractive index and absorption measurements of nonlinear optical liquids in the visible and near-infrared spectral region, Optical Materials Express **2**, 1588-1611 (2012).

[2] J. P. Gordon, R. C. C. Leite, R. S. Moore, S. P. S. Porto, and J. R. Whinnery, Long-transient effects in lasers with inserted liquid samples, J. Appl. Phys. **36**, 3-8 (1965).

[3] A. Linan and V. N. Kurdyumov, Laminar free convection induced by a line heat source and heat transfer from wires at small Grashof numbers, J. Fluid Mech. **362**, 199-227 (1998).

[4] D. P. Shelton, Polarization and angle dependence for hyper-Rayleigh scattering from local and nonlocal modes of isotropic fluids, J. Opt. Soc. Am. B **17**, 2032-3026 (2000); erratum, **34**, 1550 (2017).

[5] D. P. Shelton, Nonlocal hyper-Rayleigh scattering from liquid nitrobenzene, J. Chem. Phys. **132**, 154506 (2010).

[6] D. P. Shelton, Accurate hyper-Rayleigh scattering polarization measurements, Rev. Sci. Instrum. **82**, 113103 (2011).

1. Temperature at the laser beam focus.

The absorption coefficient for liquid water at the laser beam wavelength $\lambda = 1064$ nm is $b = 13$ m^{-1} for H_2O and $b = 1.2$ m^{-1} for D_2O [1]. Power absorbed from the focused laser beam heats the liquid, and the temperature increase at the focus is determined by thermal inertia, conduction and convection [2,3]. Thermal parameters for D_2O are collected in Table 1.

In the present experiment, the Gaussian laser beam focus in the D_2O sample, where the HRS signal is produced, has the form of a long cylinder with waist radius $w_0 = 4$ μm and confocal length $z_0 = 62$ μm. The laser produces pulses of duration 6 ns at $R = 10$ kHz repetition rate, so the pulse energy is $E = P/R = 0.20$ mJ for a laser beam with average power $P = 2.0$ W. The intensity at the center of the focused beam waist is $I = 2P/(\pi w_0^2)$.

Ref. 2 considers the temperature distribution resulting from thermal conduction of the absorbed power for a Gaussian laser beam. The thermal time scale for heat conduction [Eq. (5) from Ref. 2] is

$$t_c = w_0^2/(4D) \qquad (S1)$$

where $D = k/(\rho c_P)$ is the thermal diffusivity, k is the thermal conductivity, ρ is the density, and c_P is the heat capacity. The conduction time scale $t_c = 28$ μs is much longer than the 6 ns pulse duration, so thermal inertia determines the temperature rise during the laser pulse, with $\Delta T = Q/(\rho c_P)$ due to the absorbed energy per unit volume Q. The light intensity of the cavity-dumped laser pulse is constant during the pulse, so the temperature increases linearly during the pulse. For a beam with average power $P = 2.0$ W, ΔT increases up to $\Delta T = 2.0$ K during the pulse, and then decays until the next pulse. The average transient ΔT during the pulse is 1.0 K.

This transient ΔT during the pulse is superposed on the steady state temperature increase from the time average absorbed power, which is given by Eq. (A14) of Ref. 2 (corrected by inserting a missing π, and with heat expressed in J instead of cal)

$$\Delta T(r) = \frac{bP}{4\pi k}\left[\ln[2\gamma_1 (a/w_0)^2] - 2(r/w_0)^2\right], \qquad (S2)$$

where $\gamma_1 = e^\gamma \approx 1.781$, $\gamma \approx 0.5772$ is the Euler-Mascheroni constant, and a is the radius of the coaxial cylindrical isothermal outer boundary. Eq. (S2) is derived assuming only conductive heat transport and is a good approximation for $r/w_0 < 0.5$. The result $\Delta T(r = 0) = 0.98$ K is obtained using Eq. (S2) for an coaxial outer boundary with radius $a = 10$ μm around a laser beam with $w_0 = 4$ μm and $P = 2.0$ W.

2

The solution for ΔT including natural convection, for a heat source which is a horizontal line or wire of radius a, is given in scaled form by Eq. (4.15) from Ref. 3

$$2\pi\theta = \ln(4/U_0) - \gamma - \ln\bar{r}, \qquad\qquad (S3)$$

where $\theta = (T - T_\infty)/(T_h - T_\infty)$ is scaled ΔT, $\bar{r} = r/l_h$ is scaled r, and $U_0 = 0.87$ is the scaled fluid velocity $U = u/u_h$ at $r = 0$. Eq. (S3) is obtained for large Prandtl number (Pr > 1), and small scaled wire radius ($\varepsilon \ll 1$) and Grashof number ($Gr \ll 1$), and is valid for $\bar{r} \leq 1/\text{Pr}$. The solution in this case has an inner region of scale a where the temperature and velocity fields are dominated by heat conduction and viscosity, and a much wider outer region of width l_h where there is both conductive and convective heat transport due to the flow produced by buoyancy forces (the thermal plume). Table 2 collects the scaling and dimensionless parameters for the present problem.

Eq. (S2) is applied to calculate ΔT_1 between the center and surface of a cylinder of radius a enclosing the coaxial Gaussian beam heat source with purely conductive heat transport inside the cylinder, and Eq. (S3) is applied to calculate ΔT_2 for the surface of this cylinder heat source embedded in a fluid of infinite extent including conduction and convection. The sum $\Delta T_1 + \Delta T_2$ gives the steady state temperature increase at the laser beam focus. Choosing $a = 10$ μm gives $\Delta T_1 = 0.98$ K for the inner conductive region and $\Delta T_2 = 2.24$ K for the outer convective region, for a total 3.22 K. Adding the 1.0 K average transient increase during the laser pulse gives $\Delta T = 4.2$ K at the focus of the 2.0 W laser beam in D_2O.

Table 1. Parameters for D_2O at 25°C.

parameter	symbol	value
density	ρ	1104 kg m^{-3}
heat capacity	c_P	4.31 kJ kg^{-1} K^{-1}
thermal conductivity	k	0.607 W m^{-1} K^{-1}
thermal diffusivity	$D = k/(\rho c_P)$	1.45×10^{-7} m^2 s^{-1}
viscosity	μ	1.11×10^{-3} Pa s
kinematic viscosity	$v = k/(\rho c_P)$	1.01×10^{-6} m^2 s^{-1}
thermal expansion coefficient	$\beta = -\dfrac{1}{\rho}\dfrac{\partial \rho}{\partial T}$	2.1×10^{-4} K^{-1}
gravitational acceleration	g	9.81 m s^{-2}
absorption coefficient	b	1.2 m^{-1}
average laser beam power	P	2.0 W
abs. power / unit length	$q = bP$	2.4 W m^{-1}
abs. energy / unit volume	$Q = 2bE/(\pi w_0^2)$	9.5×10^6 J m^{-3}

Table 2. Scale and dimensionless parameters for thermal convection with q = 2.4 W m^{-1} heat from a wire of radius a = 10 μm and wire temperature $(T_w - T_\infty)$ = 2.2 K.

parameter	symbol	value
length scale	$l_h = (qg\beta/kD^2)^{-1/3}$	1.37×10^{-4} m
velocity scale	$u_h = D/l_h$	1.06×10^{-3} m s^{-1}
temperature scale	$(T_h - T_\infty) = q/k$	3.95 K
scaled wire radius	$\varepsilon = a/l_h$	0.073
Prandtl number	$\mathrm{Pr} = v/D$	6.97
Grashof number	$Gr = g\beta(T_w - T_\infty)a^3/v^2$	4.4×10^{-6}

2. Polarization analysis with large collection aperture.

The A_T, A_L and A_O mode intensities are simply related to the HRS intensities for VV, HV, VH, and HH polarization configurations at 90° scattering angle by Eqs. (1)-(6). However, HRS experiments typically use a large angular light collection aperture to increase the weak signal, and this has the effect of mixing and altering the polarized HRS signals. The signal and mixing both increase as $(NA)^2$, where the numerical aperture is $NA = n \sin \theta_A$, n is the refractive index of the medium, and θ_A is the maximum off-axis angle for collected light. The desired signals for $\theta = 90°$ scattering angle can be obtained by using a very small angular aperture or by making measurements for successively smaller apertures and extrapolating to zero angular aperture. In the present work the polarized HRS signals were collected with a large numerical aperture, and A_T, A_L and A_O mode intensities for $\theta = 90°$ scattering angle were obtained by inverting the relations for the measured HRS intensities at the experimental NA.

Expressions for the HRS intensities I_{VV}, I_{HV}, I_{VH} and I_{HH} produced by A_T, A_L and A_O modes are given in Refs. 4 and 5 as functions of the scattered ray direction θ, ψ, where θ is the spherical polar angle measured from the incident light direction [5]. The ray directions measured from the collection optic axis are given by the in-plane and out-of-plane angles $\phi = \theta - 90°$ and ψ, and the measured HRS signals are the sum over the collection aperture of the contributions from all the collected rays, taking into account reflection and refraction along the optical path. The rays from a source point in the liquid propagate to the exit face of the silica glass cuvette, to the collimating lens, to the circular aperture which sets the numerical aperture for light collection, and finally to the linear polarizer which selects the light polarization. The effect of Fresnel reflection at the cuvette exit face and collimation by the lens is to rotate the linear polarization of the incident ray by an angle

$$\alpha = \arctan[(T_\perp(\beta)/T_\parallel(\beta))^{1/2} \sin\phi \sin\psi /(\cos\phi + \cos\psi)] \tag{S4}$$

where $T_\perp$ and $T_\parallel$ are the Fresnel transmission coefficients for the components polarized parallel and perpendicular to the plane of incidence, and $\beta = \arccos(\cos\phi \cos\psi)$ is the angle of incidence on the cuvette face [5].

Integrating over ϕ, ψ for NA = 0.375 gives the following result for VV, HV and VH+HH intensities for D_2O in the present apparatus

$$\begin{pmatrix} VV \\ HV \\ VH + HH \end{pmatrix} = \begin{pmatrix} 1.47475 & 8.61941 & 0.0389339 \\ 0.999558 & 1.09758 & 0.0368772 \\ 1.98975 & 1.06134 & 1.05654 \end{pmatrix} \begin{pmatrix} A_O \\ A_T \\ A_L \end{pmatrix}. \tag{S5}$$

5

This relation can be inverted to give

$$\begin{pmatrix} A_O \\ A_T \\ A_L \end{pmatrix} = \begin{pmatrix} -0.1633 & 1.32119 & -0.040097 \\ 0.143218 & -0.215791 & 0.00225428 \\ 0.163671 & -2.2714 & 1.01974 \end{pmatrix} \begin{pmatrix} VV \\ HV \\ VH + HH \end{pmatrix}.$$ (S6)

The uncertainties for A_T, A_L and A_O are obtained by propagating the $\sqrt{N}$ statistical uncertainty for photon count N for the VV, HV, VH, and HH measurements. The relative statistical uncertainties are increased by the partial cancellation of terms in Eq. S6, with the largest effect for A_L. This estimate does not account for other error sources such as laser intensity fluctuations or errors in the numerical aperture and scattering angle, but photon count fluctuations are usually the main uncertainty for weak HRS signals. Experimental methods used to make accurate HRS polarization measurements are described in Ref. 6.

The accuracy of Eq. (S6) is tested by calculating A_T, A_L and A_O from measurements of HRS intensity ratios I_{VV}/I_{HV}, I_{HV}/I_{VH}, and I_{HH}/I_{VH} at $NA = 0.375$, then using these values of A_T, A_L and A_O to calculate HRS intensity ratios I_{VV}/I_{HV}, I_{HV}/I_{VH}, and I_{HH}/I_{VH} as a functions of NA, including values at $NA = 0$. These calculated ratios can be compared to direct measurements at several NA, and also to the $NA = 0$ results obtained by extrapolation to $NA = 0$ using the measurements at several NA. This comparison is shown in Figures 1 and 2 for two typical cases. The examples in Figures 1 and 2 show that the intensity ratios change about 10% over this range of NA, and there is agreement to about 1% for intensity ratios at $NA = 0$ obtained using Eq. (S6) and by empirical extrapolation.

Figure S1. HRS polarization ratios I_{VV}/I_{HV}, I_{HV}/I_{VH}, and I_{HH}/I_{VH} versus $(NA)^2$ measured for D_2O at $\nu = 0$ cm^{-1} with 4.2 cm^{-1} bandwidth. The solid curves are based on the results of Eq. (S6) applied to the points at $(NA)^2 = 0.1407$ ($NA = 0.375$), while the dashed curves are polynomial fits to the measurements at all three NA values.
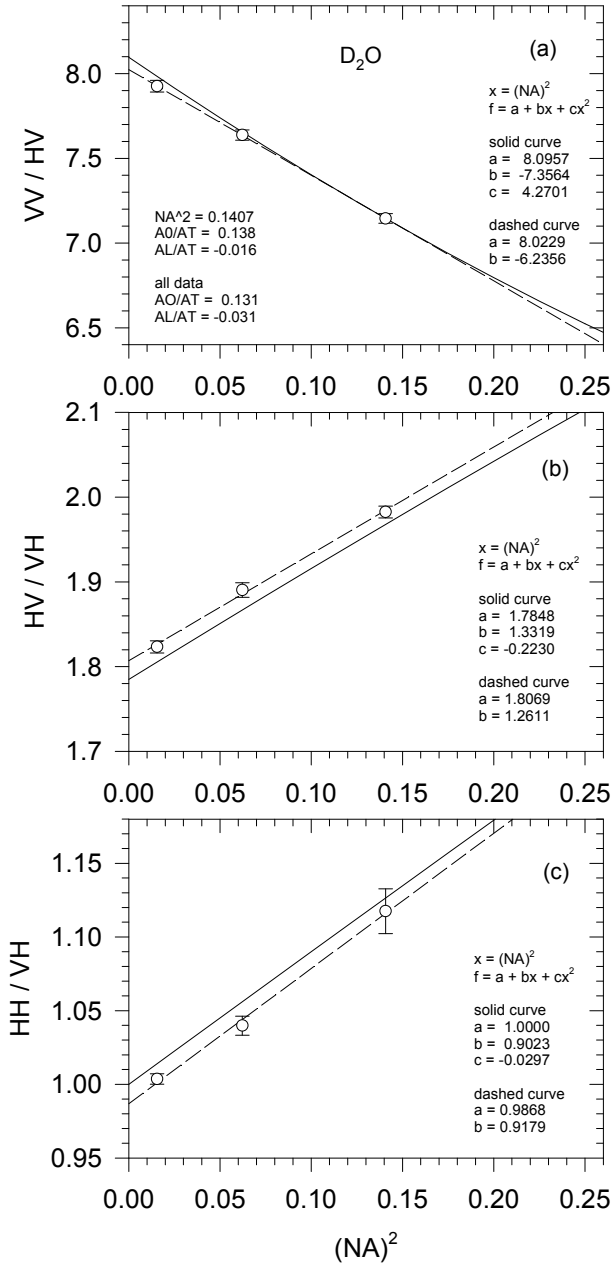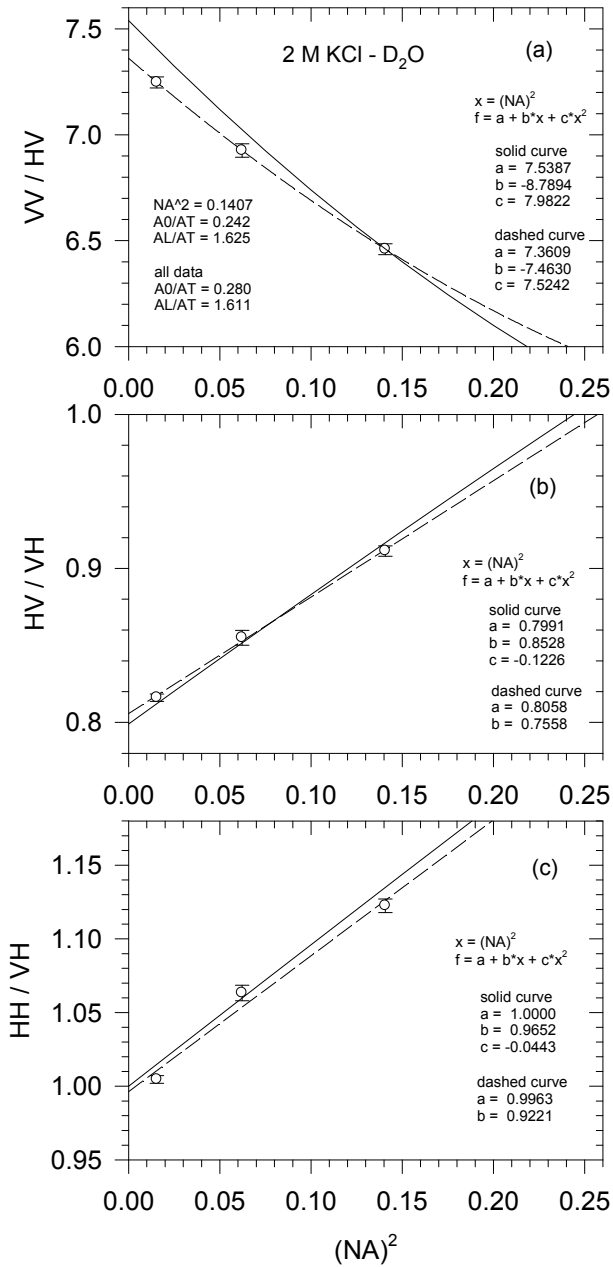
Figure S2. HRS polarization ratios I_{VV}/I_{HV}, I_{HV}/I_{VH}, and I_{HH}/I_{VH} versus $(NA)^2$ measured for 2 M KCl – D$_2$O at $\nu = 0$ cm^{-1} with 4.2 cm^{-1} bandwidth. The solid curves are based on the results of Eq. (S6) applied to the points at $(NA)^2 = 0.1407$ ($NA = 0.375$), while the dashed curves are polynomial fits to the measurements at all three NA values.

3. HRS spectra and fit functions.

The HRS spectra for D_2O contain features with spectral width ranging from < 1 cm^{-1} to >100 cm^{-1}. The spectral slit width (SSW) for the scanning spectrometer (Jobin-Yvon U1000 Ramanor) was set to 1, 4 or 20 cm^{-1} FWHM (full width at half maximum height) according to the feature being scanned. The actual function fit to the measured spectrum is the convolution of the normalized spectrometer spectral slit function with the constructed HRS spectral intensity function.

The spectrometer spectral slit function was measured by scanning the frequency-doubled (using a KTP SHG crystal) single mode laser output at λ = 532 nm (100 MHz FWHM). The expected profile (in the geometric optics limit) is triangular or trapezoidal according to whether the exit slit width is equal to or wider than the entrance slit of the grating spectrometer. Figure S3 shows measurements and fits for 1, 4 and 20 cm^{-1} SSW.

The simple triangular and trapezoidal fit functions in Fig. S3 deviate from the experimental measured intensities by about 10% at the corners. These deviations have no significant effect on the convolved fit function when the spectrum is broader than the SSW. However, the systematic deviations seen in Figure S3 will appear in the fit to the HRS spectrum for a narrow peak scanned with wide SSW. This can result in residuals for the weighted least squares fit much larger than the statistical uncertainties, and χ^2 much larger than expected for a good fit. The expected value of χ^2 for a fit with residuals only as large as the statistical uncertainties of the data is $\chi^2 = n_{DOF} \pm \sqrt{2n_{DOF}}$, where $n_{DOF} = n_{pts} - n_{param}$ is the number of degrees of freedom for n_{pts} data points and n_{param} adjustable fit parameters. For a peak with 10^5 photon counts per data point and 0.3% statistical uncertainty, each data point with 10% residual contributes 1000 to the sum for χ^2. The fits to spectra with a wide SSW scan of a narrow peak use the width of the narrow spectral function determined from a scan with smaller SSW, so the fit returns reliable results for the adjustable peak position and intensity parameters despite the high value for χ^2.

Figure 4 shows examples of the polarized HRS data. The A_T, A_L and A_O intensities at each frequency shown in Figures S5 – S8 are obtained from Figure S4, using Eq. (S6) to combine the I_{VV}, I_{HV}, I_{VH} and I_{HH} data points at that frequency, and then correcting these intensities using the spectral response function for the spectrometer. The spectral results in Figures S9 – S12 are similarly obtained.

The A_T, A_L and A_O spectra are fit using functions constructed as sums of Lorentzian or Gaussian functions. The fit parameters are the intensity, position and width for each component function. The nominal frequency shift in the recorded spectrum is x. The frequency shift origin is calibrated using the laser second harmonic generated with a KTP crystal, but the spectrometer calibration can drift. The fitted peak position x_1 for the

hyper-Rayleigh peak serves as an internal reference to determine the actual $v = 0$ cm^{-1} position, and $x - x_1$ is used as the frequency shift for spectra which include the hyper-Rayleigh peak. For spectra which do not have the hyper-Rayleigh peak as an internal reference, x is used for the frequency shift.

The sum of Lorentzian functions fit to the data in Figures S5 – S8 is the sum of a central Lorentzian peak f_{L1} and pairs of Stokes and anti-Stokes peaks given by f_{Lj} for j = 2 to m, where m varies from 6 to 9. The variable $x - x_1$ is the Raman shift, and the fit parameters A_{Lj}, x_j and w_{Lj} are the peak intensity, position and width for the j-th peak. The position for zero Raman shift is determined from the position of the central peak of the T mode spectrum. The width of the central Lorentzian w_{L1} is determined from the spectra in Figures S9 and S10 acquired with higher resolution.

The fit function for Figures S5 - S8 has the sum of functions

$$f_{L1} = A_{L1}/(1+[(x-x_1)/w_{L1}]^2) \tag{S7a}$$

$$f_{L2} = A_{L2}/(1+[(x-x_1-x_2)/w_{L2}]^2)$$
$$+ A_{L2}/(1+[(x-x_1+x_2)/w_{L2}]^2) \tag{S7b}$$

$$f_{L3} = A_{L3}/(1+[(x-x_1-x_3)/w_{L3}]^2)$$
$$+ A_{L3}/(1+[(x-x_1+x_3)/w_{L3}]^2) \tag{S7c}$$

$$f_{L4} = A_{L4}/(1+[(x-x_1-x_4)/w_{L4}]^2)$$
$$+ A_{L4}/(1+[(x-x_1+x_4)/w_{L4}]^2) \tag{S7d}$$

$$f_{L5} = A_{L5}/(1+[(x-x_1-x_5)/w_{L5}]^2)$$
$$+ A_{L5}/(1+[(x-x_1+x_5)/w_{L5}]^2) \tag{S7e}$$

$$f_{L6} = A_{L6}/(1+[(x-x_1-x_6)/w_{L6}]^2)$$
$$+ A_{L6}/(1+[(x-x_1+x_6)/w_{L6}]^2) \tag{S7f}$$

$$f_{L7} = A_{L7}/(1+[(x-x_1-x_7)/w_{L7}]^2)$$
$$+ A_{L7}/(1+[(x-x_1+x_7)/w_{L7}]^2) \tag{S7g}$$

$$f_{L8} = A_{L8}/(1+[(x-x_1-x_8)/w_{L8}]^2)$$
$$+ A_{L8}/(1+[(x-x_1+x_8)/w_{L8}]^2) \tag{S7h}$$

$$f_{L9} = A_{L9}/(1+[(x-x_1-x_9)/w_{L9}]^2)$$
$$+ A_{L9}/(1+[(x-x_1+x_9)/w_{L9}]^2) \tag{S7i}$$

The Stokes/anti-Stokes asymmetry is accounted for by the Boltzmann factor

$$f_B = 1/(1+\exp[-(x-x_1)hc/k_BT]) \tag{S8}$$

with $(hc/k_BT)^{-1} = 207$ cm^{-1} at 25°C. The fit function f_1 given by

$$f_1 = (f_{L1} + f_{L2} + f_{L3} + f_{L4} + f_{L5} + f_{L6} + f_{L7} + f_{L8} + f_{L9})f_B \qquad \text{S9}$$

is convolved with the 20 cm^{-1} FWHM trapezoidal spectral slit function from Figure S4(c) and fit to the data. The error bars for the weighted least squares fit are the propagated photon counting statistical uncertainties. Parameters values and error bars for the fits are shown in Figures S5 and S7. Fit parameters shown without error bars were not adjusted in the fit.

Figure S9 shows the D$_2$O HRS spectrum for $v < 10$ cm^{-1} acquired with 1.24 cm^{-1} SSW. The fit function has a central Lorentzian peak on a flat background. Over this range the flat background adequately represents the spectral fit in Figure S5 with the central Lorentzian deleted. The spectral slit function for the convolution in Fig. S9 is the triangle in Fig. S3(a) broadened into a 1.24 cm-1 FWHM trapezoid by the spectrometer origin drift during the 17 hour data acquisition time. The fit function for Figure S9 is the convolution of f_1 with a 1.24 cm^{-1} trapezoid, where

$$f_1 = (f_{L1} + B)f_B \; , \qquad (S10)$$

f_{L1} is given by Eq. (S7a), B is the flat background, and f_B is given by Eq. (S8). The fit in Figure S9(b) determines the width $w_{L1} = 0.554 \pm 0.005$ cm^{-1} of the central Lorentzian for the dipole orientation mode of D$_2$O. The relative integrated intensities for the central Lorenzian components in Figure S9 are $A_O / A_T = 0.171 \pm 0.017$ and $A_L / A_T = 0.003 \pm 0.025$.

Figure S10 shows the spectrum for $v < 100$ cm^{-1} acquired with 4.2 cm^{-1} SSW. The spectrum is fit with a function which is the sum of a central Lorentzian peak and a background given by the scaled fit function from Figure S5 with the central Lorentzian deleted. The fit function for Figure S10 is the convolution of f_1 with the 4.2 cm^{-1} triangle spectral slit function from Fig. S4(b), where

$$f_1 = (f_{L1} + A_{LR}f_R)f_B \; , \qquad (S11)$$

f_{L1} is given by Eq. (S7a), f_R is the fit function from Figure S5 with the central Lorentzian deleted, A_{LR} is the scale factor, and f_B is given by Eq. (S8). The width $w_{L1} = 2.21 \pm 0.08$ cm^{-1} of the central Lorentzian for the octupolar orientation mode of D$_2$O is determined by the fit in Fig. S10(a). The relative integrated intensities for the central Lorentzians of the O, T and L orientation modes for D$_2$O determined from the spectral fits in Figure S10 are $A_O / A_T = 0.170 \pm 0.010$ and $A_L / A_T = 0.017 \pm 0.006$.

Figure S11 shows the spectrum for the bending mode at 1215 cm^{-1} fit by a function which is the sum of two Lorentzians. The fit function for Figure S11 is the convolution of f_1 with a 20 cm^{-1} trapezoid, where

$$f_{L1} = A_{L1}/(1+[(x-x_1)/w_{L1}]^2) \tag{S12a}$$

$$f_{L2} = A_{L2}/(1+[(x-x_2)/w_{L2}]^2) \tag{S12b}$$

$$f_B = 1/(1+\exp[-xhc/k_BT]) \tag{S13}$$

$$f_1 = (f_{L1}+f_{L2})f_B . \tag{S14}$$

Figure S12 shows the spectrum for the stretching mode at 2500 cm^{-1} fit by a function which is the sum of five Gaussians. The fit function for Figure S12 is the convolution of f_1 with a 20 cm^{-1} trapezoid, where

$$f_{G1} = A_{G1}\exp(-[(x-x_1)/w_{G1}]^2) \tag{S15a}$$

$$f_{G2} = A_{G2}\exp(-[(x-x_2)/w_{G2}]^2) \tag{S15b}$$

$$f_{G3} = A_{G3}\exp(-[(x-x_3)/w_{G3}]^2) \tag{S15c}$$

$$f_{G4} = A_{G4}\exp(-[(x-x_4)/w_{G4}]^2) \tag{S15d}$$

$$f_{G5} = A_{G5}\exp(-[(x-x_5)/w_{G5}]^2) \tag{S15e}$$

$$f_B = 1/(1+\exp[-xhc/k_BT]) \tag{S16}$$

$$f_1 = (f_{G1}+f_{G2}+f_{G3}+f_{G4}+f_{G5})f_B . \tag{S17}$$

Figure S13 shows the VV HRS spectrum for D$_2$O measured over a 3500 cm^{-1} range. The curves for the A_O, A_T and A_L spectral functions in Figure S13 are the sum of the corresponding fit functions from Figures S5, S11 and S12, for the libration, bending and stretching bands, scaled by factors 1.15, 0.85 and 1.00, respectively. The scaling accounts for the different laser power during data acquisition for each spectral band. The VV spectral curve obtained from the A_O, A_T and A_L spectral functions using Eq. (S5) is convolved with the 20 cm^{-1} trapezoid from Figure S3(c) to produce the VV HRS curve in Figure 13.

Figure S3. Spectrometer spectral slit functions obtained by scanning the frequency-doubled (using a KTP SHG crystal) single mode laser output at $\lambda = 532$ nm.
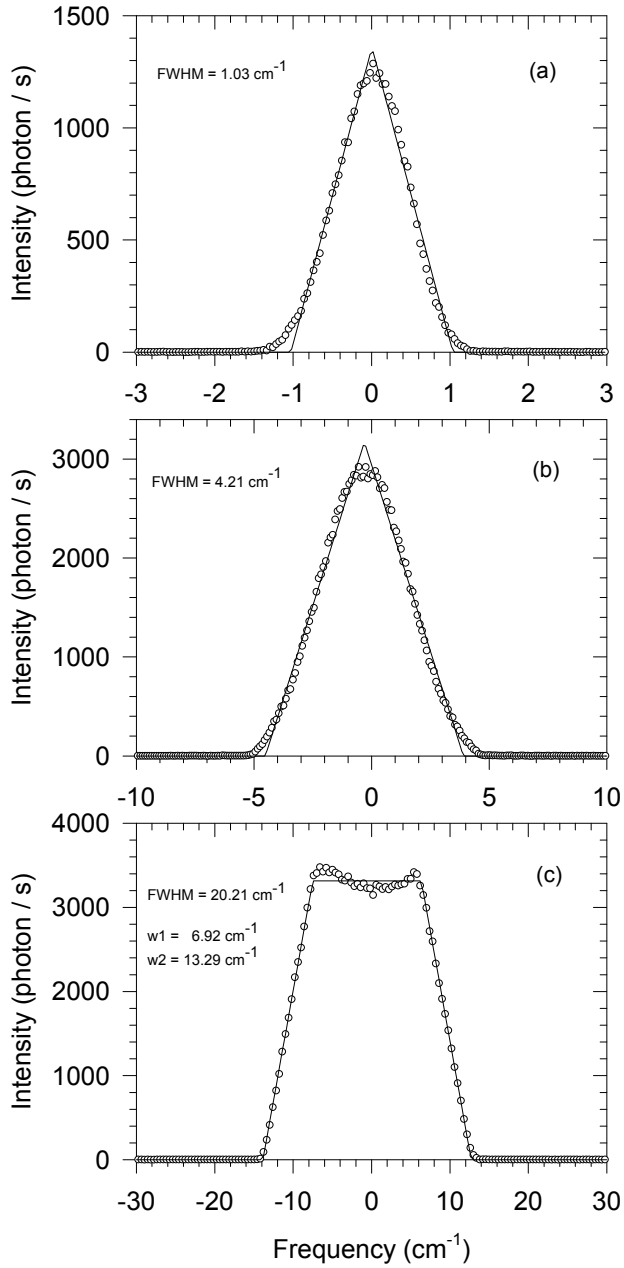
Figure S4. Polarized HRS spectra obtained from 140 repeats of the VV, HH, VH, HH spectrum scan sequence, with 20 cm^{-1} SSW, 250 points per spectrum and total acquisition time 280 s per point. The intensity outside the central peak decreases from VV (black curve) highest, then HH (red) and VH (green), with HV (blue) lowest. The intensities for HH and VH spectra differ, with $I_{HH} \approx 1.1 \times I_{VH}$, because of the large collection numerical aperture $NA = 0.375$. At most one photon produced during a laser pulse is counted by the detector, so the dead time corrected photon count rate is $\widetilde{S} = -R \ln(1 - S/R)$ where S is the measured photon count rate and R is the laser pulse repetition rate. The octupolar (O), transverse dipolar (T) and longitudinal dipolar (L) spectra in Figures S5 – S8 are obtained by combining the dead time corrected VV, HH, VH and HV polarized HRS spectra.
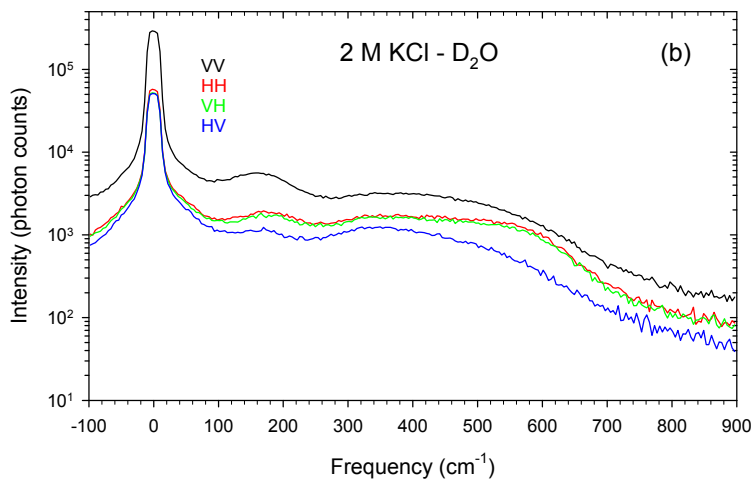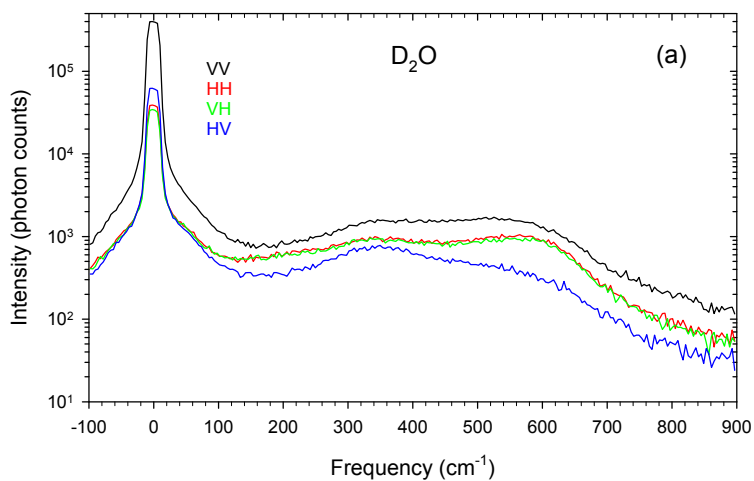
Figure S5. Fits to D_2O spectra (20 cm^{-1} SSW) with logarithmic intensity scale and fit parameters.
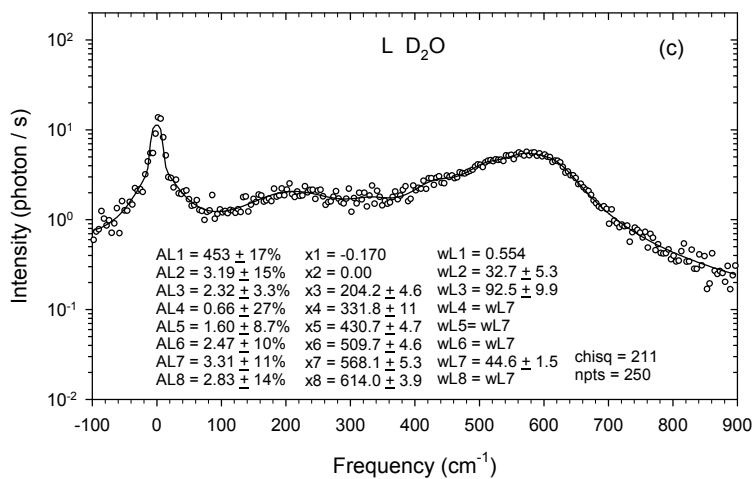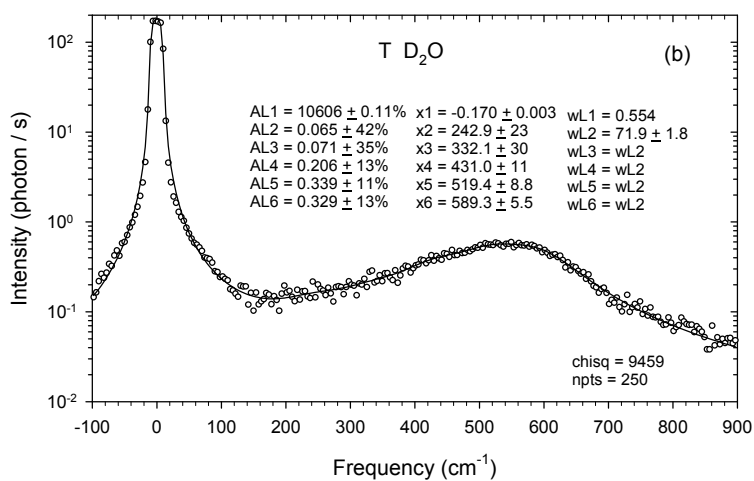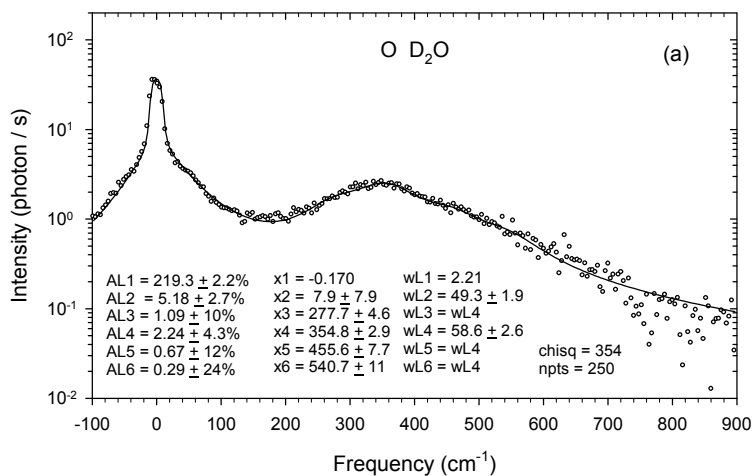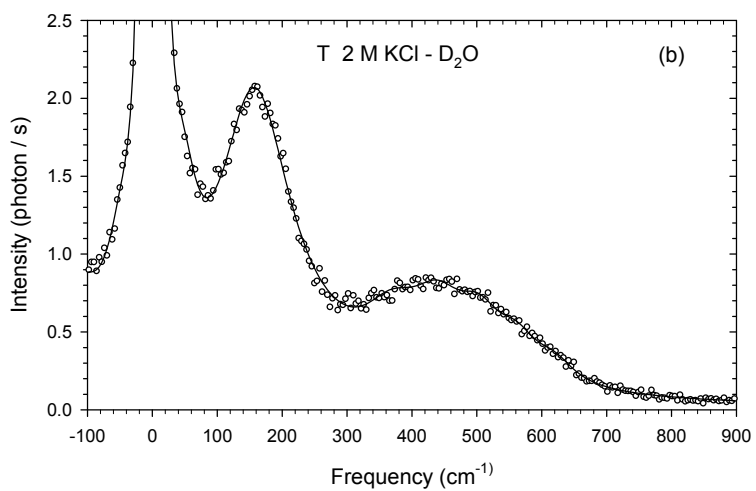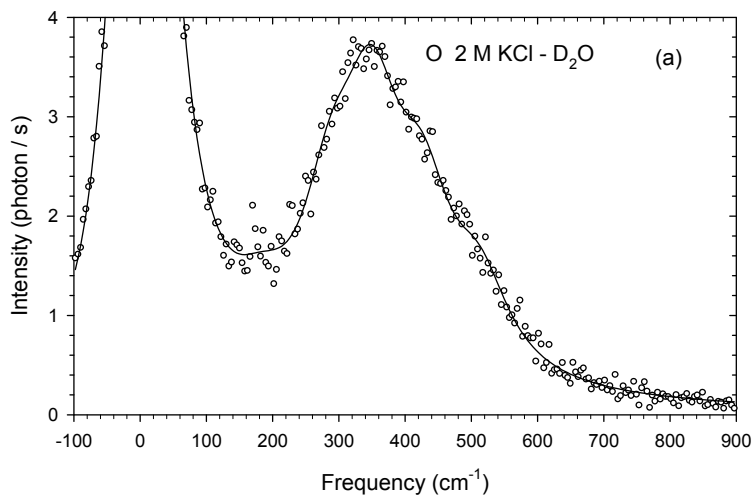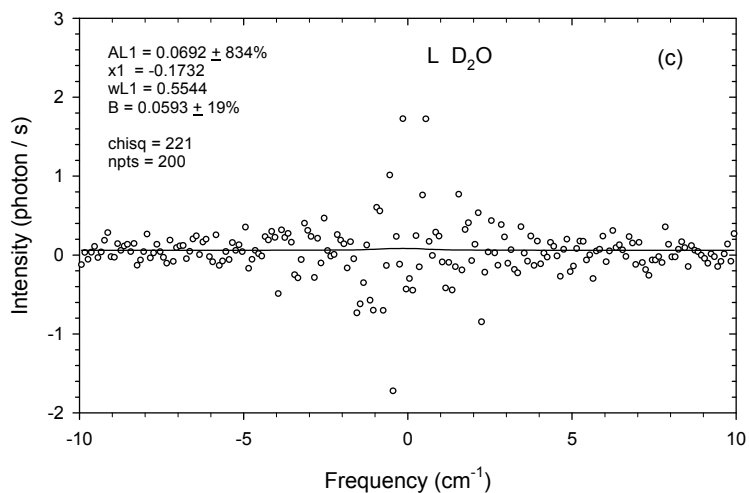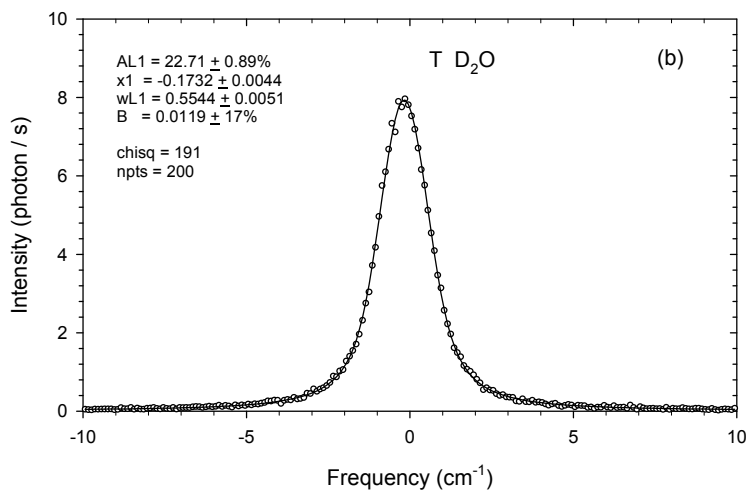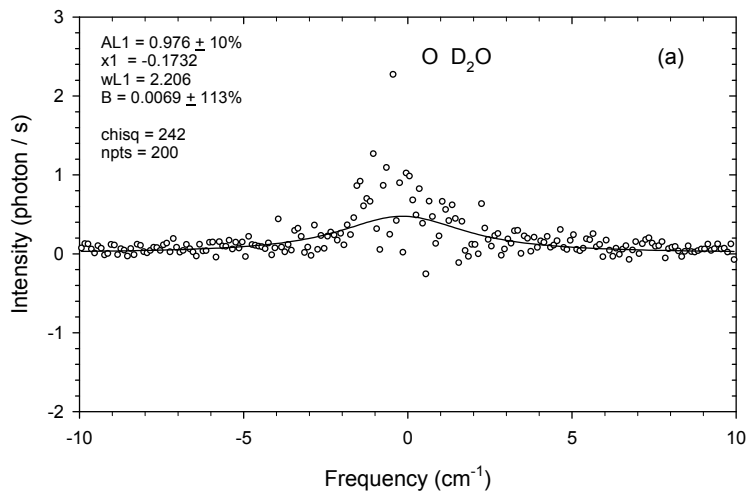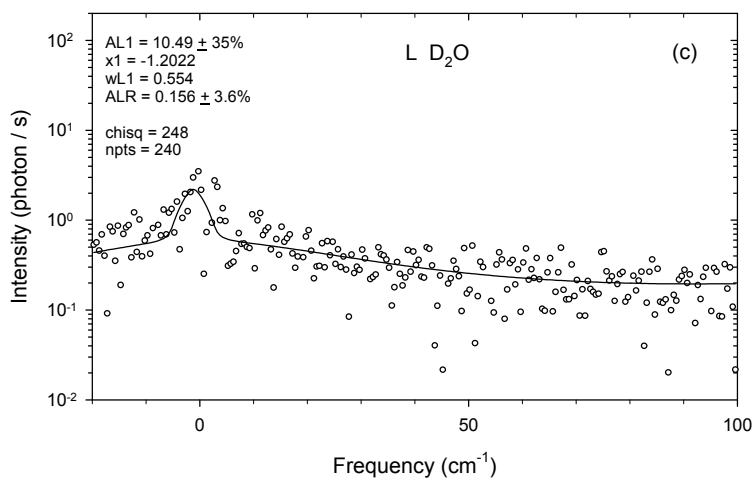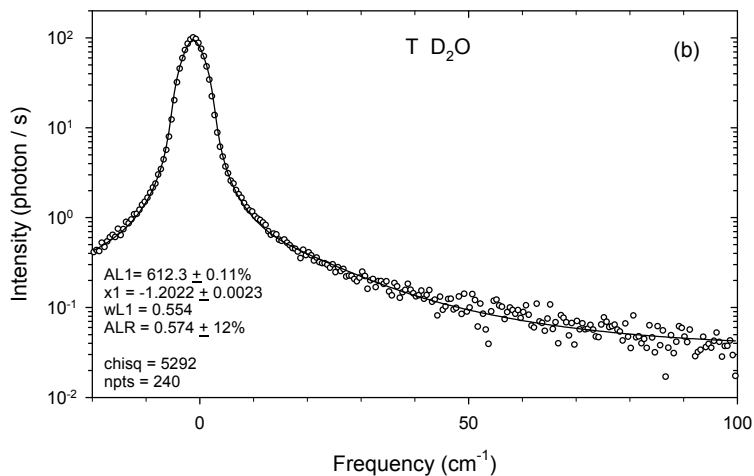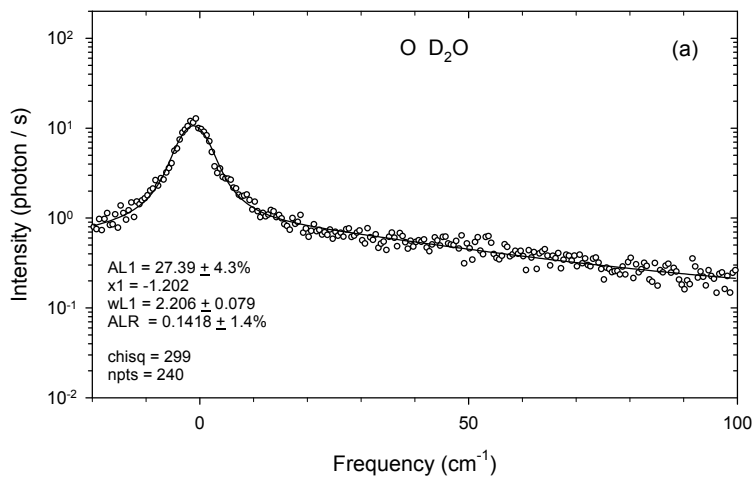
Figure S6. Fits to D_2O spectra (20 cm^{-1} SSW) with linear intensity scale.
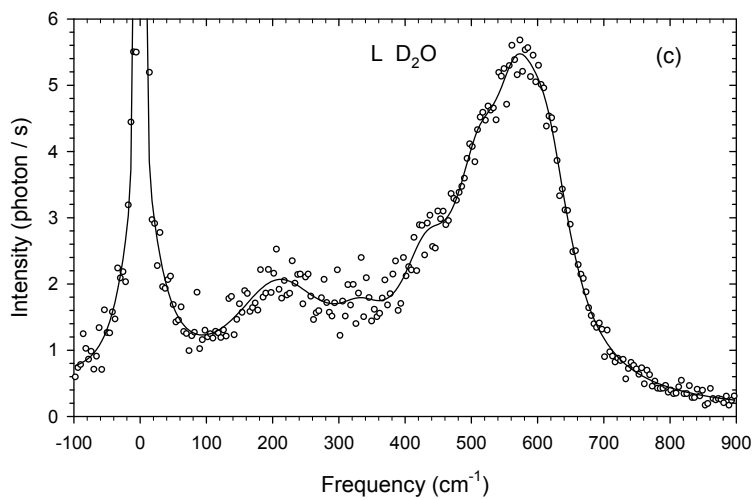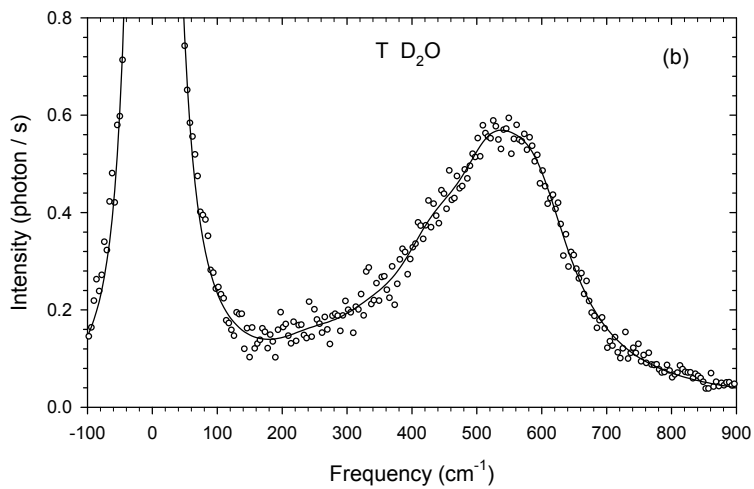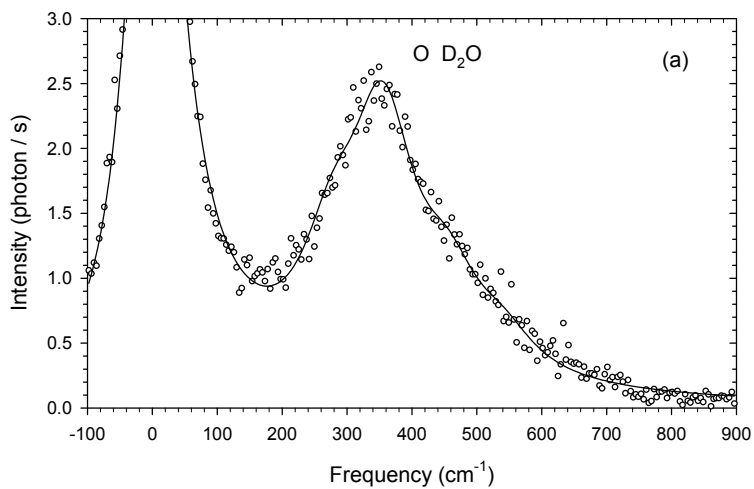
Figure S7. Fits to 2 M KCl - D_2O spectra (20 cm^{-1} SSW) with logarithmic intensity scale and fit parameters.
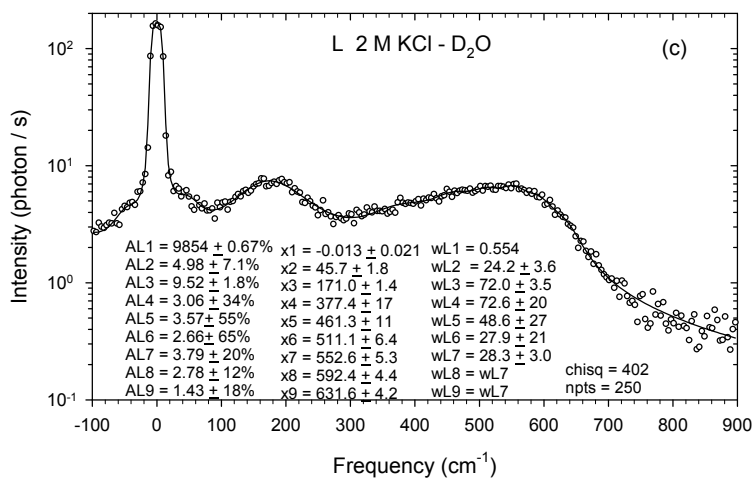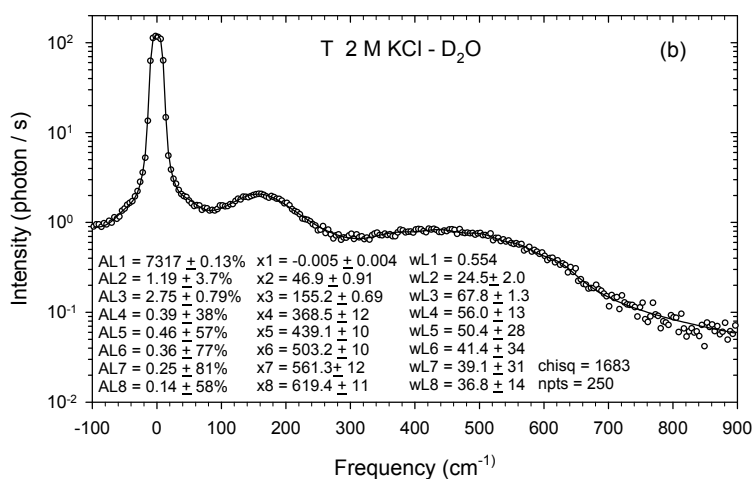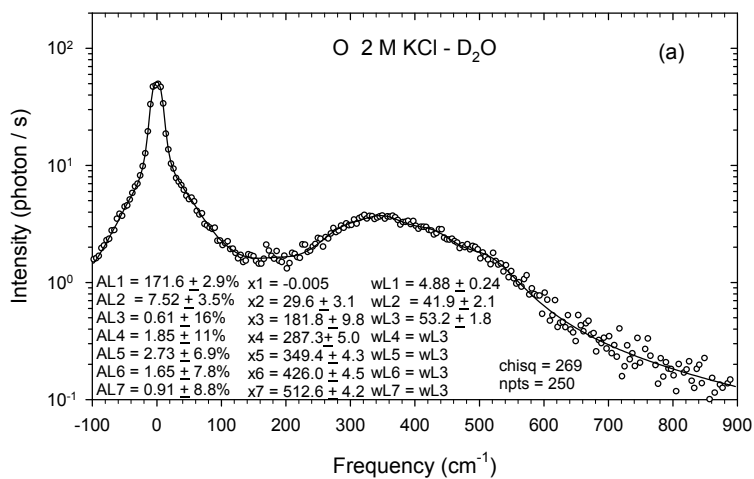
Figure S8. Fits to 2 M KCl - D$_2$O spectra (20 cm^{-1} SSW) with linear intensity scale.
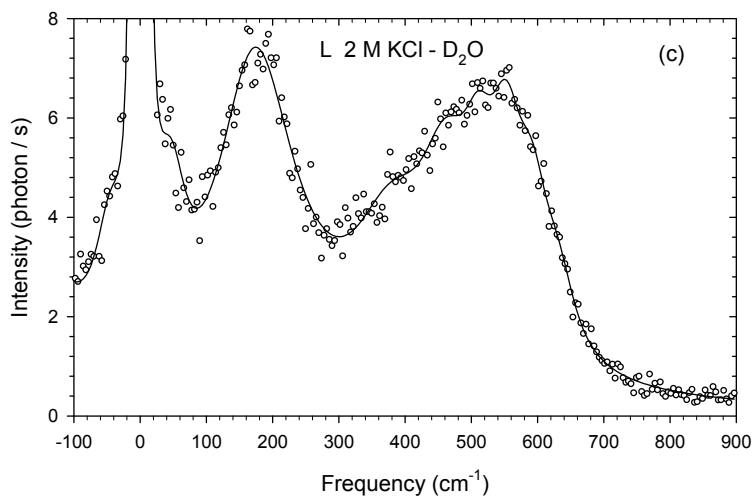
Figure S9. Fits to D$_2$O spectra (1.24 cm^{-1} SSW) with linear intensity scale.

(a) O D$_2$O

AL1 = 0.976 ± 10%
x1 = -0.1732
wL1 = 2.206
B = 0.0069 ± 113%

chisq = 242
npts = 200

(b) T D$_2$O

AL1 = 22.71 ± 0.89%
x1 = -0.1732 ± 0.0044
wL1 = 0.5544 ± 0.0051
B = 0.0119 ± 17%

chisq = 191
npts = 200

(c) L D$_2$O

AL1 = 0.0692 ± 834%
x1 = -0.1732
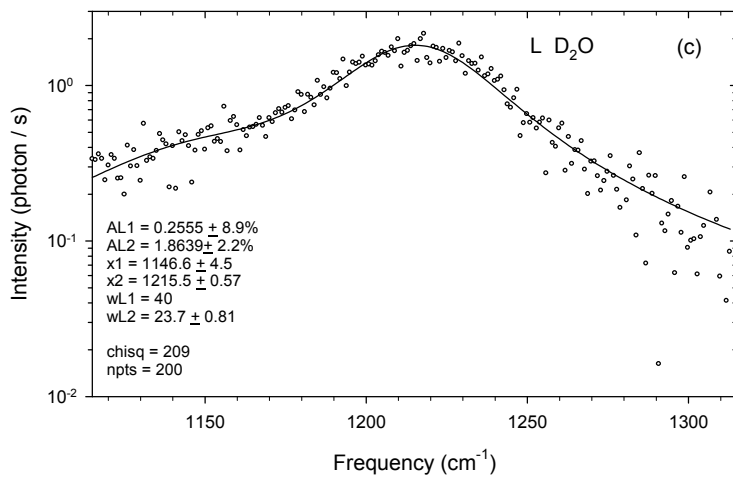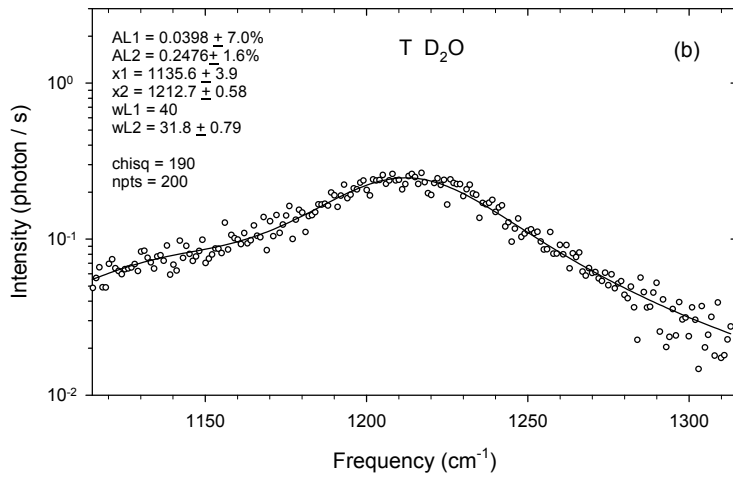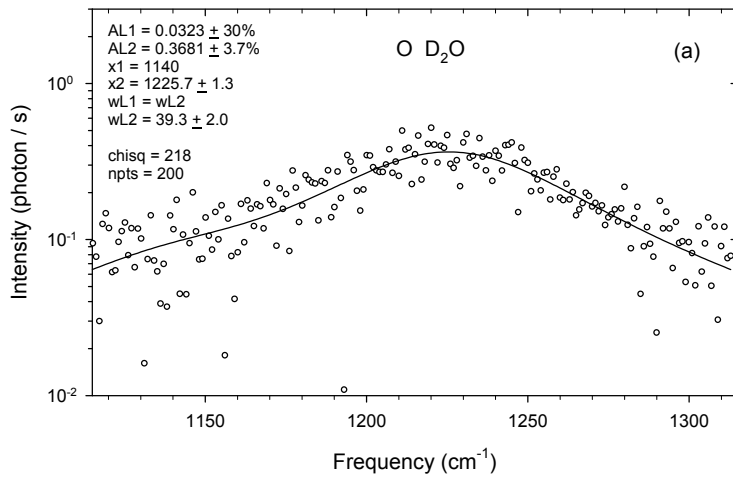wL1 = 0.5544
B = 0.0593 ± 19%

chisq = 221
npts = 200

Figure S10. Fits to D_2O spectra (4.2 cm^{-1} SSW) with logarithmic intensity scale.

O D_2O (a)

AL1 = 27.39 ± 4.3%
x1 = -1.202
wL1 = 2.206 ± 0.079
ALR = 0.1418 ± 1.4%

chisq = 299
npts = 240

T D_2O (b)

AL1= 612.3 ± 0.11%
x1 = -1.2022 ± 0.0023
wL1 = 0.554
ALR = 0.574 ± 12%

chisq = 5292
npts = 240

L D_2O (c)

AL1 = 10.49 ± 35%
x1 = -1.2022
wL1 = 0.554
ALR = 0.156 ± 3.6%

chisq = 248
npts = 240

Figure S11. Fits to D$_2$O spectra (20 cm^{-1} SSW) with logarithmic intensity scale.

Figure S12. Fits to D_2O spectra (20 cm^{-1} SSW) with logarithmic intensity scale.
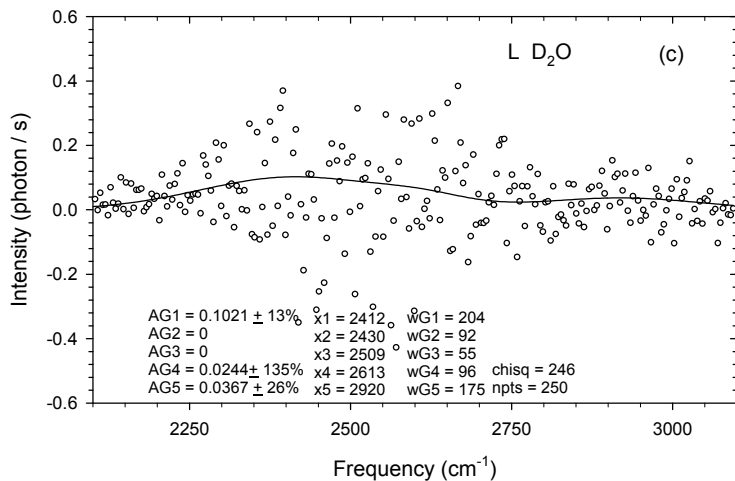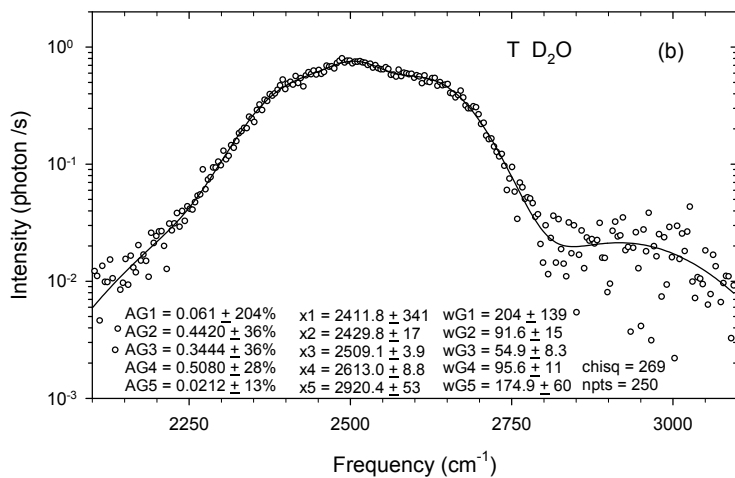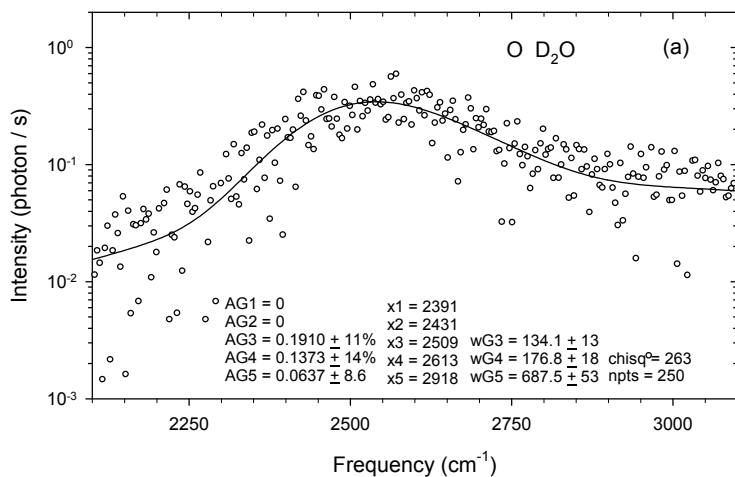
Figure S13. VV HRS spectrum for D_2O (20 cm^{-1} SSW) with data points and fitted curve on a logarithmic intensity scale. The VV (black) curve is constructed from the O (green), T (blue) and L (red) spectral mode curves.